Available online at www.sciencedirect.com
SCIENCE DIRECT®
Journal of Non-Crystalline Solids 351 (2005) 3347–3355
JOURNAL OF NON-CRYSTALLINE SOLIDS
www.elsevier.com/locate/jnoncrysol

Structure of bioactive mixed polymer/colloid aerogels

Luis Esquivias [a,*], Víctor Morales-Flórez [a], Manuel Piñero [b], Nicolás de la Rosa-Fox [a]

[a] Departamento de Física de la Materia Condensada, Facultad de Ciencias, Universidad de Cádiz, 11510 Puerto Real, Spain
[b] Departamento de Física Aplicada, CASEM, Universidad de Cádiz. 11510 Puerto Real, Spain

Received 11 January 2005

Abstract

The structure of polymer/colloid mixed silica sono-aerogels has been studied by SAXS, N_2 adsorption–desorption and Hg porosimetry. The system is described as a composite in which the polymeric phase (sonogel) is the matrix. The structure of this phase prepared with ultrasounds is very fine consisting in aggregates of ~5 nm radius formed by elementary particles of 1 nm radius. Including Ca(II) into the silica atomic network causes enlarging the average size of the particle more than three times with respect to its size in its pure silica counterpart. The stiffness increases as well by 50%. The size of the particles and pores is also affected by the ultrasound dose applied; the higher for the larger the particles. On the other hand, a low dose produces a rough particle surface.

PACS: 81.05.Je; 81.05.Rm; 81.20.Fw; 82.20.Wt

1. Introduction

The combination of two particulate materials with a processing that allows full intermingling of both structures has driven our interest in polymer/colloid hybrid gels [1,2]. The material was described as a composite in which the polymeric gel is the matrix and the colloid particles, the reinforcing phase. We verified that adding colloid silica particles to TEOS-based alcogels enables the network porous volume and pore radius to be tailored. This is a very attractive feature when the inclusion of a second phase into the pores is intended with the purpose of a complete sintering of the resulting composite. The porous structure also features the performance and applications of these materials, especially attractive to prepare materials for implants since it must permit the specimens to better get infiltrated and vascularized. In a preliminary approach, we have used this combination polymer/colloid to prepare aerogels given that this characteristic is enhanced by drying the gel under supercritical conditions.

In vitro bioactivity of this material has been promoted by adding calcium to the initial sol to obtain SiO_2–CaO/SiO_2 composite. The bioactive performance must be improved by a high surface/volume ratio, which is characteristic of the sono-aerogels [3]. On the other hand, one of the effects of ultrasonic treatment for obtaining mixed oxide gels is favoring the homogeneity at a molecular level. Bioactivity is manifested by growth of hydroxycarbonateapatite (HCA) nano-crystals that wraps the material when it is immersed in blood plasma. HCA layer is also formed when bioactive materials are soaked in solutions mimicking the features of plasma. These are so-called in vitro assays of bioactivity, a common tool in the development of new biomaterials, where HCA formation is monitored.

Ca(II) is a well known modifier of the glasses atomic network [4]. This modification induces as well changes in the gel structure that are unknown. It is the aim of this paper to simulate the structure of mixed polymer/colloid SiO_2–CaO/SiO_2 aerogels. Structural simulation turns out to be the culmination of a strategy to get the clues to act on the processing to tailor specific structures. The simulation of the aerogels structure has been approached from several points of view. The structure formation

* Corresponding author. Tel.: +34 956 01 6321; fax: +34 956 01 6288.
E-mail address: luis.esquivias@uca.es (L. Esquivias).

0022-3093/$ - see front matter © 2005 Elsevier B.V. All rights reserved.
doi:10.1016/j.jnoncrysol.2005.08.007

process has been studied by molecular dynamics technique [5], using the Feuston–Garofalini potential, concluding that the structure formation starts with a slow growing process of the clusters, followed by faster growth of the structure due to the cluster–cluster aggregation. Other authors mainly face their work to the making of characterization programs for the porous structures generated by simulation use the Monte Carlo method [6]. Gelb and Gubbins apply the Lennard–Jones potential for each element, and the Lorenz–Berthelot rules for mixing the inter-element potential. On the other hand, it has attracted interest reproducing the formation and growing processes of the aerogels by computer, with the reaction or diffusion limited cluster aggregation (RLCA or DLCA) algorithms, or some modification of them [7], or the ballistic cluster–cluster aggregation [8].

Ma et al. [9] have used structures generated with DLCA-modified algorithms characterizing them by their fractal dimension, to achieve the scale law exponent and present some models to explain the structure–properties relationship [10]. As for Woignier et al., they have worked with DLCA-generated structures, introducing a new technique for characterizing these porous systems [11]. They conclude that the pore size distribution and the hydroxyl content are relevant for describing and understanding the mechanical properties of these materials [12].

We have simulated the structure of dense gels by random close packing (RCP) models [13] from which some information about the microstructure of the gel can be obtained by using theses models [14]. Applying RCP structural models the existence of several typical sizes is manifested, whereas the USAXS (ultra small X-ray scattering) tests [15] shows a hierarchy-ordered structure. In this paper this structural approach, thoroughly described in former papers [2,16,17], has been applied.

2. Experimental procedure

2.1. Synthesis of the gels

This structural study was done on monolithic polymer/colloid mixed sono-aerogels containing silica particles. The synthesis method is based on that proposed by Toki et al. [18]. The colloidal silica selected was Aerosil-OX-50 (Degussa). According to manufacturer's specifications, the product is constituted by particles 40 nm of primary average size and exhibits 50 m^2/g of specific surface area. The percentage by weight of SiO_2 particles to total SiO_2 was 30 and 54.

The sols were elaborated by hydrolysis and polycondensation of tetramethoxysilane (TMOS) under acidic conditions (pH $[HNO_3] = 1.5$). A device delivering to the system 0.6 W cm^{-3} of ultrasound power was employed [19]. The total dissipated was 150 J cm^{-3}. Then the colloid phase was added under vigorous stirring until a homogeneous mix is obtained. Next, the pH was raised up to 4.5 by adding diluted NH_4OH. The homogeneous liquids were poured in glass hermetic containers at 50 °C until gelation. Supercritical drying [20] was performed in autoclave ($T = 260$ °C, $P = 90$ bar) following the procedure already described [21]. There were also prepared two counterparts of the sample containing 30% weight of colloid particle adding the amount necessary of $Ca(NO_3)_2$ to have a final product containing 3% weight of Ca, the difference between them is the ultrasound dose applied. These samples were named respectively 30A (dose applied 310 J cm^{-3}) and 30B (dose applied 520 J cm^{-3}).

2.2. X-ray scattering

X-ray scattering measurements were performed in a Siemens D500 diffractometer equipped with conventional Bragg–Brentano geometry and a Cu anticathode. The Cu K_α line ($\lambda = 0.1542$ nm) was selected by a bent graphite monochromator in the diffracted beam.

To cover a wide range of the scattering vector modulus $q = 4\pi \sin\theta/\lambda$, where θ is the half scattering angle and λ the selected wavelength, two series of data were collected: one series at small angle (SAXS) for $0.3° < \theta < 10.0°$ ($0.3\ nm^{-1} < q < 7\ nm^{-1}$) with steps of 0.02° to obtain information about dispersion entities of correlation lengths included between 20 and 0.9 nm. Other series were obtained for $10.0° < \theta < 90.0°$ with steps of 0.04 °C to determine the presence of traces of crystallization.

Porod's limiting law for SAXS

$$\lim\left[\frac{I(q)q^4}{Q_0}\right] = \frac{S}{V}\frac{1}{\pi\phi(1-\phi)}, \tag{1}$$

enables the quantity S/V to be calculated irrespective of the geometric distribution of the phases even in the absence of well define particles [22], where Q_0 is the integrated intensity

$$Q_0 = \int_0^\infty I(q)q^2\,dq \tag{2}$$

and S and V are, respectively, the surface and the volume of one of the two phases of volume fraction ϕ. These aerogels exhibit a positive deviation from the Porod's law due to electronic density fluctuation at the pore–solid interface. Positive deviation from Porod's law leads to no constant but linear relationship Iq^4 with the scattering angle

$$\lim[I(q)q^4] = A + Bq^4, \tag{3}$$

where A is the Porod constant, and B the corresponding intensity fluctuation. This parameter is a measure of the deviation from the Porod's law, associated with electronic density fluctuations due to the solid phase microporosity. On the other hand, the parameter A is strongly related to the surface roughness of the solid–pore interface network.

Another important parameter that can be tested is the mean chord length given by

$$l_c = \frac{4Q_0}{\pi A}. \tag{4}$$

Table 1
Structural parameters of the models from our catalogue employed in this work

	K_{max}	C	ρ_{RCP} (g/cm^3)	V_{RCP} (cm^3/g)	V_m (cm^3 of mesopore/g)	N_{CM}
H0L7	0.31	0.58	1.28	0.33	0.31	7.66
H0L8	0.22	0.59	1.29	0.32	0.27	8.53
H0L9	0.28	0.61	1.34	0.29	0.27	8.87
HP20L10	0.38	0.47	1.03	0.52	0.35	7.05

K_{max} is the distribution maximum position; C is the packing fraction; ρ_{RCP} is model specific mass in the case of being formed by silica particles; V_{RCP} is the specific volume of the model (RCP); V_m the specific mesopore volume, i.e., after subtracting the volume of the pores larger that the particle size; N_{CM} is the particle average coordination number.

This parameter represents the harmonic average of the pore and solid chord, which may be considered as the weighted average size of both phases

$$\frac{1}{l_c} = \frac{1}{l_p} + \frac{1}{l_s}. \quad (5)$$

2.3. Transmission electron microscopy

For transmission electronic microscopy, samples were stored over holy carbon films held in 3 mm diameter circular cooper grid. Film preparation was done following typical procedure [23]. For storing the sample on the holy carbon film, grids were dove in an *n*-hexane suspension of the sample. This way, some drops of this suspension are allowed to be collected, and after the solvent evaporation, some particles of the sample stay stored over the grid. Images were taken in a JEOL JEM-1200EX at 120 kV, with a guaranteed resolving power of 0.2 nm lattice.

The actual Ca content of sample 30A and 30B was determined by EDX resulting to be $(3.2 \pm 0.5)\%$ weight.

2.4. Nitrogen physisorption

The gels were texturally characterized by isothermal nitrogen adsorption–desorption at 77 K in an automatic device. Pore size distributions were calculated from the desorption branch by the Barret–Joyner–Halenda (BJH) method [24] and the specific surface by Brunauer–Emmet–Teller (BET) method.

2.5. Mercury intrusion porosimetry

To asses the mechanical behavior under isostatic compression and resolve larger pore size, where N_2 physisorption is not reliable, porosity was also characterized by mercury intrusion on de-gassed monolithic composites, according the procedure already described [1]. Hg pressure varied from 0.1 to 390 MPa. After the run, the samples presented both compaction and intruded mercury.

3. Structural approach

The gel structure is depicted as a collection of packed spherical particles [13] and models are built on the 'solid space' based on this premise. Then, we extract its 'pore space' feature and created a catalogue of pore size distributions according different condition of particle coordination number and compaction. The models are represented as a function of the variable $K = r/R$, where r is the radius of the largest inscribed sphere in the interstice and R the radius of the particles. Finally, pore distributions can be compared to the experimental measurement. A logarithmic scale for K is used to make easier the fitting of the experimental data, simply sliding it along the K-axis until the position considered giving the best fit. Given the maximum, the fit allows the particle size of a mono-disperse system to be calculated from the maxima of the pore size distributions. From the distribution of each one of these contributions to the experimental distribution, successive sizes and local densities of hierarchic distribution may be deduced [25]. Data on the pore volumes associated with different hierarchical levels, size of aggregates, the local density of the *i*th aggregation level, and packing of the successive levels can be obtained. Table 1 accounts for the structural parameters of every particular model of our catalogue used in this paper.

4. Results

4.1. SAXS

The Fig. 1 represents the intensities of the radiation scattered by the samples 54 and 30 in a log–log scale, as a function of the scattering vector q. Going towards the low-q

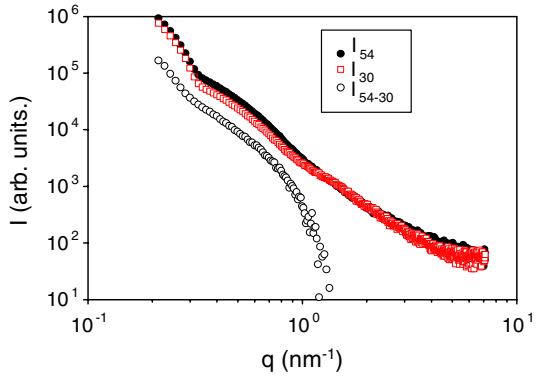

Fig. 1. SAXS curves for 54 (full dots) and 30 (white squares) composites aerogels. The difference between their scattered intensities is represented below.

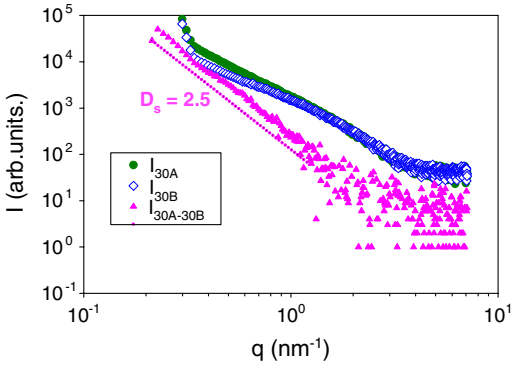

Fig. 2. SAXS curves for 30A (full dots) and 30B (white diamonds) composites aerogels with added Ca(II). The difference between their scattered intensities is represented below (full triangles).

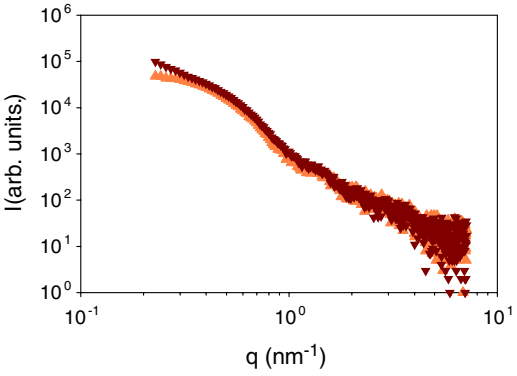

Fig. 3. SAXS curves of the difference between 30 and 30A data (dark triangles) and 30B (light triangles) composites sono-aerogels. The difference between their scattered intensities is represented below.

region, the mixed polymer/colloid sono-aerogel patterns present an increasing intensity, related with the heterogeneities at this level; as it maybe expected, they are quite alike. To extract more information about their structural dissimilarities, we have subtracted their intensities. This curve accounts for unshared structural features. It takes only values significantly different up to $q \approx 1\ \mathrm{nm}^{-1}$. In this case, the contributions of the finest part of the structure are removed, typically the elementary particles of the sonogel phase and their nano-aggregates indicating a similar structure in both samples at this level. The difference indicates the presence of larger scatterers in the 54 than in 30 sample, whether pores or solid particles.

In the same way, in Fig. 2, it can be seen the intensities scattered by the samples with added Ca 30A and 30B, which differs only in the dose of applied ultrasound energy during their processing; so as to investigate the effect of the ultrasound dose on the gel structure these intensities have been subtracted. It presents a linear regime of slope $m = -3.5$ along one decade permitting describe this effect in terms of surface fractality of dimension $D_s = 2.5$ accounting for the effect of ultrasounds on the particle surface roughness. On the other hand, the X-ray diffraction patterns at wide angle ($7.1 < q < 57\ \mathrm{nm}^{-1}$) are coincident, presenting no structural differences at an atomic level.

This last effect can be seen by the difference between the intensities scattered by the samples 30 and 30A besides the difference between 30 and 30B represented in Fig. 3. These curves inform about the modification on the sonogel structure produced by the incorporation of the Ca into the silica atomic network. The difference between them basically lies as before, on the shortest q region.

The value calculated for the parameters described in Section 2 are included in Table 2.

4.2. TEM

In Figs. 4–6 it can be seen the structural differences between the sample containing Ca and the pure silica composite. The addition of Ca influences deeply not only the atomic structure, as it must be expected, but also the texture of the resulting aerogel. In sample 30, colloidal particles can be distinguished from the polymerized TEOS matrix. This is formed by a uniform distribution of sphere-like particles randomly packed of 4–5 nm mean

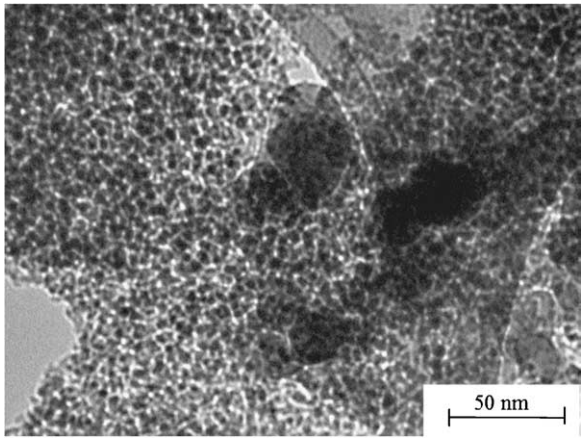

Fig. 4. Micrography of the 30 sample where it can be seen the fine structure of the sonogel with some aerosil particles.

Table 2
Structural parameter calculated from SAXS, picnometry and N_2 physisorption

	Q_0 (nm^{-3})	d_a ($\mathrm{g/cm}^{-3}$)	M (Mpa)	$\lim[I(q)q^4]$	Φ_s	V/S (nm)	S' (m^2/g)	S_{BET} (m^2/g)	l_c (nm)	l_s (nm)	l_p (nm)
54	6300	0.382	21.4	$15800 + 52.24q^4$	0.17	0.9	840	126	0.5	0.6	3.0
30	5100	0.424	18.9	$8323 + 51.8q^4$	0.19	1.3	520	95	0.8	1.0	4.1
30A	6240	0.391	25.4	$3441 + 38.21q^4$	0.19	3.6	630	39	2.3	2.9	12
30B	5590	0.359	29.4	$2437 + 41.03q^4$	0.18	5.0	583	65	2.9	3.6	16

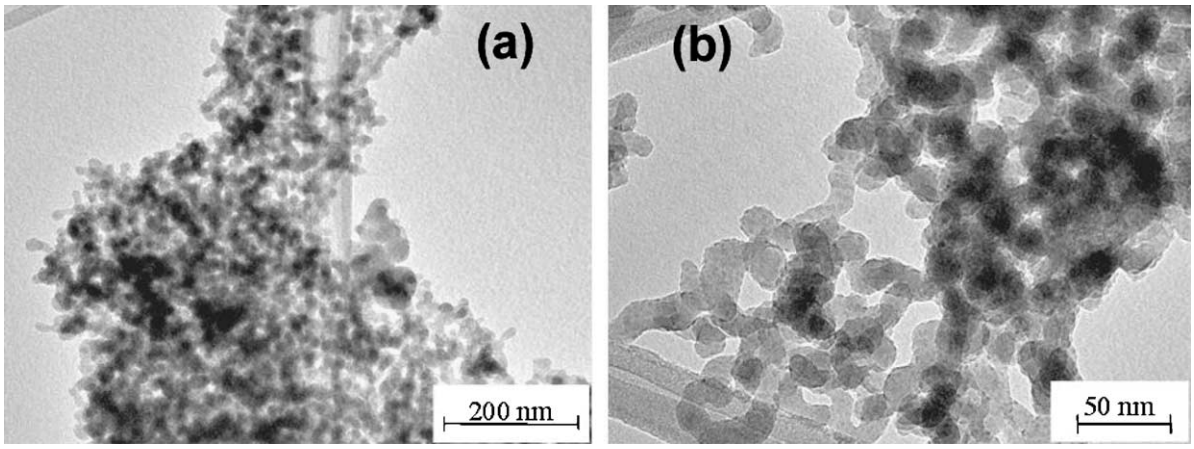

Fig. 5. TEM micrographies of the sample 30A. It can be described as a uniform distribution of spherical particles (a). There it can be observed a distribution of spherical particles, larger than in the case of its pure silica counter part (Fig. 4). Rod-like parts forming pores of tenths of nm can also be observed (b).

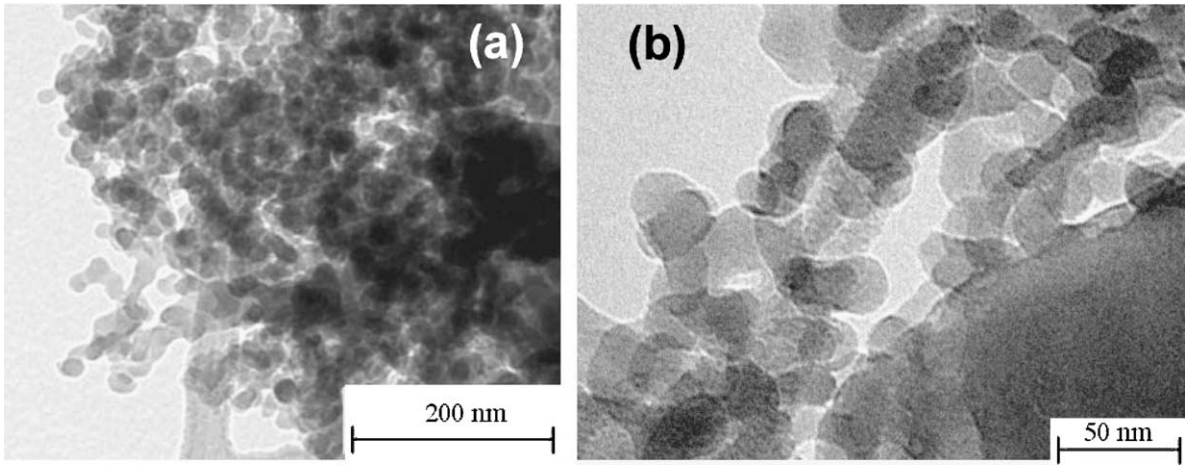

Fig. 6. TEM micrographies of the sample 30B. Similar as can be seen in sample A, uniform distribution of sphere-like and rod-like particles can be observed here (a). However, sample B does not show golf ball-like surface (b).

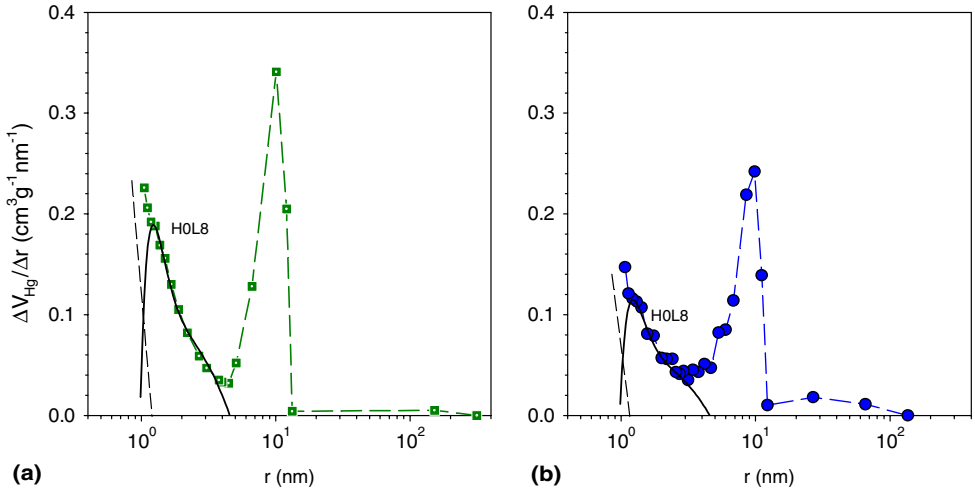

Fig. 7. Pore volume distribution of the sample 54 (a) and 30 (b). Bold lines correspond to the applied model. Dashed line below $r = 1$ nm describes the tail of the micropores distribution. The particle radius can be estimated from the tail. Lines between symbols are eye guides.

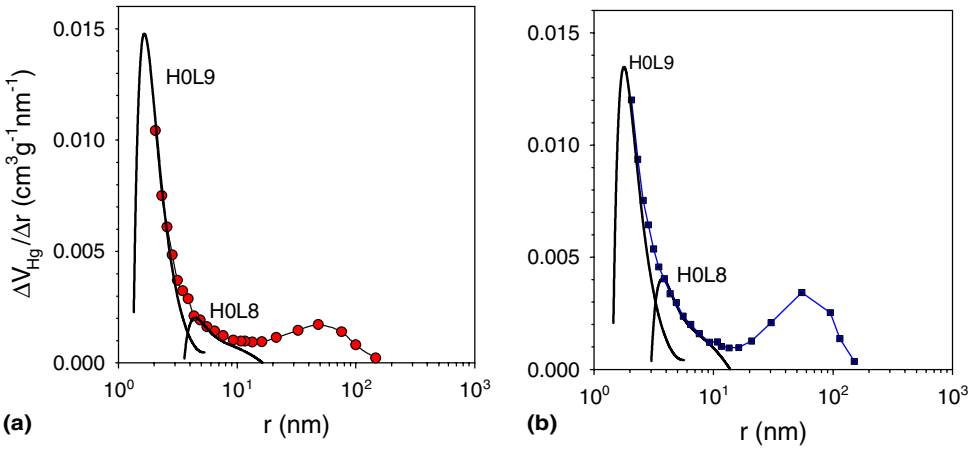

Fig. 8. Pore volume distribution of the sample 30A (a) and 30B (b). Bold lines correspond to the applied model.

Table 3
Structural parameters of the sono-aerogels, calculated from the applied models

Sample	Level 1				Level 2						
	Model	r_0	ρ_1	V_1	Model	r_1	ρ_2	V_2	ρ_2^*	C_2^*	V_2^*
54	–	~1.1	–	–	H0L8	4.8	1.79	0.14	1.31	0.60	0.31
30	–	~1.1	–	–	H0L8	4.8	1.58	0.21	1.31	0.60	0.31
30A	H0L9	6.2	1.96	0.055	H0L8	17	1.85	0.010	–	–	–
30B	H0L9	6.1	1.92	0.025	H0L8	15	1.86	0.016	–	–	–

r_i (nm), ρ_i (g cm^{-3}), V_i (cm^3/g of composite), V_i^* (cm^3/g of sonogel).

radius. There it can be observed isolated big colloidal particles embedded into the matrix. The Ca containing aerogel (Figs. 5 and 6) presents a matrix structure less particulate but rod-like, forming whether floppy or interconnected branches of 6 nm size. In the sample 30A with lower ultrasound dose, the surface is not smooth but it has the aspect of a golf ball. Scattered domains with the same texture than the observed in pure silica sample are found throughout the sample.

4.3. N_2 physisorption

The pore distributions (Figs. 7 and 8) are quite similar. They present a well-defined feature in the range of pores radius smaller than 5 nm that overlaps with the micropores distribution (the tails of which are sketched with dashed lines). An interesting result is that the quotient between the specific volumes calculated for distributions is found to be in agreement with ratio 46/70, i.e., the relative contents on sonogel phase. This part of the distributions can be satisfactorily described with the model H0L8, as it is shown. They exhibit as well a peak at ~10 nm caused by the colloidal particles. These particles are decorated with sonogel giving rise to narrow pore size distribution that has not the condition under which our models were built up.

The density of the *i*-level can be calculated as

$$\rho_i = \left(V_i + \frac{1}{\rho_s}\right)^{-1}, \qquad (6)$$

where ρ_s is the elementary particle density and V_i is the pore specific volume at the *i*-level (analytically calculated). Thus, we have referred the measured volume to the amount of sonogel of the corresponding sample, V_i^*, that permits to calculate the particular density ρ_i^* of the sonogel phase at the level *i*. Then, the density of the composite is calculated as the weighted average of both phases, considering that at this level of resolution the density of the colloid phase is that of the bulk silica, i.e., 2.2 g cm^{-3}.

Concerning the samples containing Ca, they present a peak at ~2 nm with a long queue that can be resolved with the models H0L9 and H0L8. In both cases, an extent distribution is found between 20 and 120 nm, likely due to the pore formed by large structural units of Ca containing par-

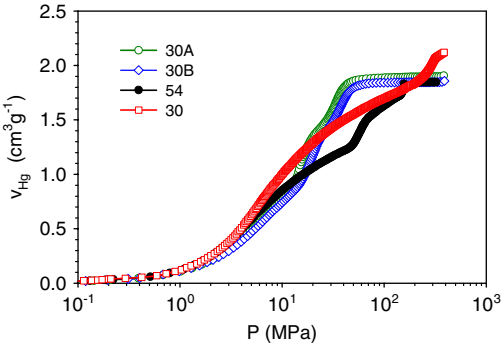

Fig. 9. Hg intrusion curves.

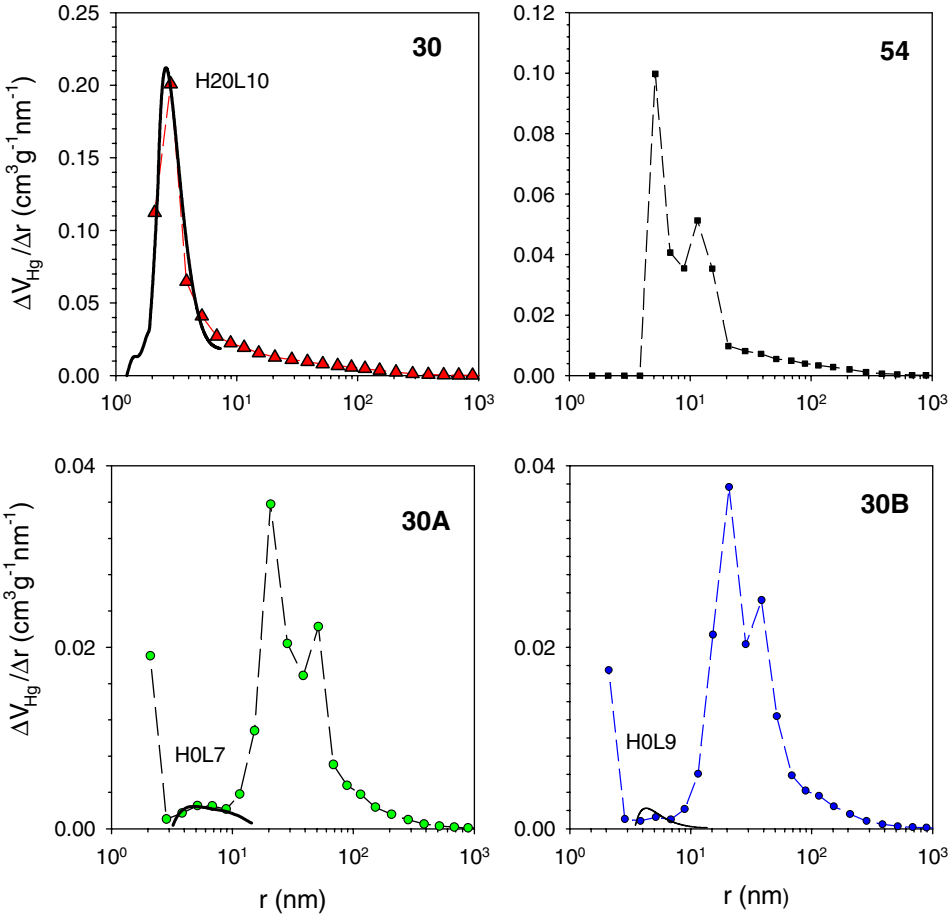

Fig. 10. Pore size derivatives obtained from Hg intrusion porosimetry. Dots correspond to the experimental data; the dashed lines between them are guide for the eyes only. Full lines are the pore distribution of the applied models.

ticles (Fig. 5). Between 15 and 40 nm it is found a distribution of pores, the fitting of which is difficult and not necessary to extract the major structural information. The calculated structural information can be found in Table 3.

4.4. Mercury intrusion

Mercury intrusion curves are represented in Fig. 9 and the pore size derivatives resulting from Hg intrusion are shown in Fig. 10. The distributions are affected by a background corresponding to the compaction of the sample caused by the isostatic pressing. The effect of this compaction is increasing the pore derivative for increasing applied pressure. This is reproduced in the graph as a fake pore distribution in the rank above the threshold of intrusion of which is complicate to extract the actual volume intruded. In all the cases, volume reduction is above 30% for 10 MPa, but the relative increase of the pore derivative tends asymptotically to zero. For this reason the reproduction of peaks is only feasible at the high pressure (low pore size) extent and there it can be observed well defined features.

The sample 30 presents a neat peak that can be fitted satisfactorily by the model H20L10 from our catalog. The long tail that follows corresponds to the compression without intrusion. The calculated structural parameters appear in Table 4.

Table 4
Structural parameters calculated from the models applied to the pore size distribution from Hg intrusion

Sample	ρ_a	Level 1				Level 2			
		Model	r_1	ρ_1	V_1	Model	r_2	ρ_2	V_2
30	1.42	H20L10	10.6	1.24	0.103	–	–	–	–
54	1.52	–	–	–	–	–	–	–	–
30A	1.50	–	~3–4	1.44	0.027	H0L7	16	1.42	0.008
30B	1.08	–	~3–4	1.05	0.030	H0L9	17	1.04	0.005

r_i (nm), ρ_i (g cm^{-3}), V_i (cm^3/g of composite), ρ_a (g cm^{-3}) is the density under an isostatic pressure of 390 MPa.

The pore volume distribution of the sample 54 presents two features that abides by particle of ~20 nm radius, contrary to what it results for the sample 30 in which the size rather corresponds to agglomerates of sonogel particles. The pore of the sonogel structure collapse.

The pore volume distributions of the Ca containing samples present their major feature at larger pore radius than the pure silica samples. The more important feature of these distributions is found between 20 and 80 nm, presenting two peaks that corresponds to a distribution of particles ~70 nm. They show as well a shoulder for $3\text{ nm} < r < 8\text{ nm}$ that, in the case of the sample 30A, it can be reproduced by the model H0L7. For the sample 30B, this feature is smaller than in the preceding case and it can be replicated by the model H0L9. Both 30A and 30B pore distributions present peaks below 3 nm that are not complete because are found at the limit of the experiment. The radius of the particles that give rise to these peaks can be estimated from the position of their tails to be ~3–4 nm.

Bulk moduli (B) have been calculated from the slope of the curve V_{Hg} vs P through the linear behavior interval (up to ~4 MPa) (Table 2).

5. Discussion

The volume/surface ratio calculated from SAXS data according to the Porod's law (Table 2) is very high, one order of magnitude longer than that calculated by BET method. This indicates that the structure so fine that is inaccessible to N_2. This structure is formed by particles of ~1 nm in aggregates of ~5 nm. This result agrees with the harmonic averages of the pore and solid calculated for the aerogels 54 and 30 indicate a fine structure, with l_s of the order of 1 nm. On the other hand, the addition of Ca(II) causes enlarging the size of the particles and pores, as it indicates the Fig. 3. The average size of the solid chord considered as the particle, as it is defined by Eqs. (4) and (5), is three times larger in the sample 30A than in its pure silica counterpart. This ratio grows up to near four for the sample 30B, which was prepared applying a higher ultrasound dose. This parameter affects as well the pore–solid interface. We attribute the surface fractal dimension extracted from the difference $I_{30A} - I_{30B}$ to the golf ball-like surface observed in the sample 30A that it is not seen in the sample 30B.

The Ca(II) containing samples is described as a hierarchy structure of order 2 with particle radius of 17 and 15 nm for the samples 30A and 30B, respectively, and $r_1 = 4.8$ nm for the particles of the outer level of the pure silica samples (Table 3). These estimates are in the ratio 3.1:1 for the sample 30A, and 3.5:1 in the sample 30B. The calculated interstitial volumes of these structures are 3.8% and 5.9% of the V_m calculated for this model (Table 3) the meaning of which is the relative volume fraction of the samples occupied by such structures. As it can be deduce from SAXS data, an effect of the ultrasounds is to reduce the interstitial volume at the lowest level (particles of ~6 nm radius) from $V_1 = 0.22V_m$ to $0.10V_m$ because the number of particle of the upper level increases. The meaning of these numbers is that 22% volume and 10% volume of the samples 30A and 30B, respectively, abides by the proposed model. This reduction occurs by collapse of the pores between the smallest particles. No distribution tails of small particles ~1 nm radius are seen in Ca(II) containing samples.

The bulk modulus (M) increases when Ca(II) is added and with the applied ultrasound dose (it increases 34.4% and 55.5% for the sample 30A and 30B, respectively, respect to their pure silica counterpart); although it takes similar value for the pure silica samples. Thus, when the samples are isostatically compressed they behave differently one from another from a structural point of view. Thus, the sample 30 compacts and forms an RCP structure with agglomerates ~10 nm radius that occupies 30% of the sample volume. The rest up to 70% corresponding to the sonogel phase would be occupied by smaller aggregates, of size below the experiment resolution (2 nm). No traces of colloidal particle structure appear because the concentration of which has not attained the percolation level. On the contrary, the pore distribution of the sample 54 when it is modified by isostatic compression shows only feature of the colloidal particles superstructure.

The Ca(II) containing samples keeps their structure at their lowest level similar to that described from N_2 physisorption because of the presence of particles between 3–4 and 16–17 nm radius. However, the compression collapse partially the interstitial volume at this level that is reduced from $0.038V_m$ (sample 30A) and $0.059V_m$ (sample 30B) up to $V_2 = 0.02V_m$.

6. Conclusion

In mixed polymer/colloid silica aerogels, the structure of the polymer phase prepared with ultrasounds is very fine consisting in aggregates of ~5 nm radius formed by elementary particles 1 nm radius. No traces of colloidal particle structure appear in the sample containing 30% weight of colloidal particles but the pore distribution of the sample 54 when it is modified by isostatic compression shows only feature of the colloidal particles superstructure.

Adding 3% weight Ca(II) causes enlarging the size of the particles and pores and increasing of the stiffness. The average size of the particle increases more than three times respect to its size in its pure silica counterpart. The higher the applied ultrasound dose the larger the particles. The ultrasound dose affects as well the interface pore–solid; low dose produce a rough particle surface. Under compression Ca(II) containing samples retain a structure based on particles ~70 nm average radius.

Acknowledgments

The authors are grateful for financial support from the Spanish Government: Ministerio de Ciencia y Tecnología (Projects: MAT2001-3805 and MAT2002-0859) and Junta de Andalucía (TEP 0115). The authors are also grateful to Degussa Iberia, S.A. for supplying Aerosil OX-50 and Fernando Conde from the Universidad Complutense de Madrid, (Spain) who provided the SAXS data.

References

[1] M.J. Mosquera, M. Bejarano, N. de la Rosa-Fox, L. Esquivias, Langmuir 19 (2003) 951.
[2] L. Esquivias, N. de la Rosa-Fox, M. Bejarano, M.J. Mosquera, Langmuir 20 (2004) 3816.
[3] E. Blanco, L. Esquivias, R. Litrán, M. Piñero, M. Ramírez-del-Solary, N. de la Rosa-Fox, Appl. Organometal. Chem. 13 (1999) 399.
[4] J. Zarzycki, in: R.W. Cahn, E.A. Davis, I.M. Ward (Eds.), Glasses and the Vitrous State, Cambridge Solid State Science Series, Cambridge University Press, p. 40.
[5] K. Yamahara, K. Okazaki, Fluid Phase Equilibria 144 (1998) 449.
[6] L.D. Gelb, K.E. Gubbins, Langmuir 15 (1999) 305.
[7] A. Emmerling, J. Fricke, J. Sol–Gel Sci. Technol. 8 (1997) 781.
[8] M. Grzegorczyk, M. Rybaczuk, K. Maruszewski, Chaos Solitons Fractals 19 (4) (2004) 1003.
[9] H. Ma, J.H. Prevost, G.W. Scherer, Int. J. Solids Struct. 39 (2002) 4605.
[10] H. Ma, A.P. Roberts, J.H. Prevost, R. Jullien, G.W. Scherer, J. Non-Cryst. Solids 277 (2000) 127.
[11] J. Primera, A. Hasmy, T. Woignier, J. Sol–Gel Sci. Technol. 26 (2003) 671.
[12] T. Woignier, F. Despetis, A. Alaoui, P. Etienne, J. Phalippou, J. Sol–Gel Sci. Technol. 19 (2000) 163.
[13] J. Rodríguez-Ortega, Modelos de estructura de geles densos (Models of structure of dense gels), Ph.D. thesis, Universidad de Cádiz, Spain, 1996.
[14] L. Esquivias, J. Rodríguez-Ortega, C. Barrera-Solano, N. de la Rosa-Fox, J. Non-Cryst. Solids 225 (1998) 239.
[15] C. Marlière, T. Woignier, et al., J. Non-Cryst. Solids 285 (2001) 175.
[16] J. Rodríguez-Ortega, L. Esquivias, J. Sol–Gel Sci. Technol. 8 (1997) 117.
[17] L. Esquivias, A. Gonzalez-Pecci, J. Rodríguez-Ortega, C. Barrera-Solano, N. de la Rosa-Fox, Ceram. Trans. 95 (1998) 183.
[18] M. Toki, S. Miyashita, T. Takeuchi, S. Kanbe, A. Kochi, J. Non-Cryst. Solids 100 (1988) 479.
[19] L. Esquivias, J. Zarzycki, in: M.D. Baró, N. Clavaguera (Eds.), Current Topics on Non-Crystalline Solids, World Scientific, Singapore, 1986, p. 409.
[20] M. Prassas, J. Phalippou, J. Zarzycki, J. Mater. Sci. 19 (1984) 1656.
[21] L. Esquivias, J. Rodríguez-Ortega, C. Barrera-Solano, N. de la Rosa-Fox, J. Non-Cryst. Solids 225 (1) (1998) 239.
[22] G. Porod, Kolloid Z. 124 (1951) 83.
[23] A. Fukami, K. Adachi, J. Electron Microsc. 14 (2) (1965) 112.
[24] E.P. Barret, L.G. Joyner, P.P. Halenda, J. Am. Chem. Soc. 73 (1951) 373.
[25] L. Esquivias, N. de la Rosa-Fox, M. Bejarano, M.J. Mosquera, Langmuir 20 (2004) 3416.